

Schwarzschild and Ledoux are equivalent on evolutionary timescales

EVAN H. ANDERS,^{1,2} ADAM S. JERMYN,^{3,2} DANIEL LECOANET,^{1,4,2} ADRIAN E. FRASER,^{5,2} IMOGEN G. CRESSWELL,^{6,2} AND
J. R. FUENTES⁷

¹CIERA, Northwestern University, Evanston IL 60201, USA

²Kavli Institute for Theoretical Physics, University of California, Santa Barbara, CA 93106, USA

³Center for Computational Astrophysics, Flatiron Institute, New York, NY 10010, USA

⁴Department of Engineering Sciences and Applied Mathematics, Northwestern University, Evanston IL 60208, USA

⁵Department of Applied Mathematics, Baskin School of Engineering, University of California, Santa Cruz, Santa Cruz, CA 95064, USA

⁶Department Astrophysical and Planetary Sciences & LASP, University of Colorado, Boulder, CO 80309, USA

⁷Department of Physics and McGill Space Institute, McGill University, 3600 rue University, Montreal, QC H3A 2T8, Canada

(Received; Revised; Accepted; Published)

Submitted to ApJ

ABSTRACT

In one-dimensional stellar evolution models, convective boundaries are calculated using either the Schwarzschild or Ledoux criterion, but there is no consensus regarding which criterion to use. In this letter, we present a 3D hydrodynamical simulation of a convection zone and adjacent radiative zone, including both thermal and compositional buoyancy forces. As expected, regions which are unstable according to the Ledoux criterion are convective. Initially, the radiative zone adjacent to the convection zone is Schwarzschild-unstable but Ledoux-stable due to a composition gradient. Over many convective overturn timescales the convection zone grows via entrainment. The convection zone saturates at the size predicted by the Schwarzschild criterion, and in this final state the Schwarzschild and Ledoux criteria are equivalent. Therefore, the size of stellar convection zones is determined by the Schwarzschild criterion, except possibly during short-lived stages in which entrainment persists.

Keywords: Stellar convection zones (301), Stellar physics (1621); Stellar evolutionary models (2046)

1. INTRODUCTION

We do not understand convective boundaries in stars. There are discrepancies between models and observations of the sizes of convective cores (Claret & Torres 2018; Viani & Basu 2020; Pedersen et al. 2021; Johnston 2021), lithium abundances in solar-type stars (Pinsonneault 1997; Sestito & Randich 2005; Carlos et al. 2019; Dumont et al. 2021), and the sound speed at the base of the Sun’s convection zone (see Basu 2016, Sec. 7.2.1). Incorrect convective boundary locations can have important impacts across astrophysics such as affecting the mass of stellar remnants (Farmer et al. 2019; Mehta et al. 2022) and the inferred radii of exoplanets (Basu et al. 2012; Morrell 2020).

While convective boundary mixing (CBM) has many uncertainties, the most fundamental question is: what determines the location of convection zone boundaries? Some stellar evolution models determine the location of the convection zone boundary using the *Schwarzschild criterion*, by comparing the radiative and adiabatic temperature gradients. In other models, the convection zone boundary is determined by using the *Ledoux criterion*, which also accounts for compositional stratification (Salaris & Cassisi 2017, chapter 3, reviews these criteria). Recent work states that these criteria should be equivalent at a convective boundary according to mixing length theory (Gabriel et al. 2014; Paxton et al. 2018, 2019), but in practice these criteria are often different at convective boundaries in stellar evolution software instruments, and this has led to a variety of workarounds (Paxton et al. 2018, 2019).

As there is still disagreement regarding which stability criterion is appropriate for 1D modeling (see [Kaiser et al. 2020](#), chapter 2), insight can be gained from studying multi-dimensional simulations. Such simulations show that convection zones adjacent to a Ledoux stable region can expand by entraining material from the stable region ([Meakin & Arnett 2007](#); [Woodward et al. 2015](#); [Jones et al. 2017](#); [Cristini et al. 2019](#); [Fuentes & Cumming 2020](#); [Andrassy et al. 2020, 2021](#)). However, past simulations have not achieved a statistically-stationary state, leading to uncertainty in how to include entrainment in 1D models ([Staritsin 2013](#); [Scott et al. 2021](#)).

In this letter, we present a 3D hydrodynamical simulation that demonstrates that convection zones adjacent to regions that are Ledoux-stable but Schwarzschild-unstable will entrain material until the adjacent region is stable by both criteria. Therefore, in 1D stellar evolution models, the Schwarzschild criterion correctly determines the location of the convective boundary when evolutionary timescales are much larger than the convective overturn timescale (e.g., on the main sequence; [Georgy et al. 2021](#)). When correctly implemented, the Ledoux criterion should return the same result ([Gabriel et al. 2014](#)). We discuss these criteria in Sec. 2, describe our simulation in Sec. 3, and briefly discuss the implications of our results for 1D stellar evolution models in Sec. 4.

2. THEORY & EXPERIMENT

The Schwarzschild criterion for convective stability is

$$\mathcal{Y}_S \equiv \nabla_{\text{rad}} - \nabla_{\text{ad}} < 0, \quad (1)$$

whereas the Ledoux criterion for convective stability is

$$\mathcal{Y}_L \equiv \mathcal{Y}_S + \frac{\chi_\mu}{\chi_T} \nabla_\mu < 0. \quad (2)$$

The temperature gradient $\nabla \equiv d \ln P / d \ln T$ (pressure P and temperature T) is ∇_{ad} for an adiabatic stratification and ∇_{rad} if the flux is entirely carried radiatively. The Ledoux criterion includes the effects of the composition gradient $\nabla_\mu = d \ln \mu / d \ln P$ (mean molecular weight μ), where $\chi_T = (d \ln P / d \ln T)_{\rho, \mu}$ and $\chi_\mu = (d \ln P / d \ln \mu)_{\rho, T}$ (density ρ).

Stellar structure software instruments assume that the location of convective boundaries coincide with sign changes of \mathcal{Y}_L or \mathcal{Y}_S ([Paxton et al. 2018](#), sec. 2). The various stability regimes which can occur in stars are described in section 3 and figure 3 of [Salaris & Cassisi \(2017\)](#), but note four important regimes:

1. Convection Zones (CZs): Regions with both $\mathcal{Y}_S > 0$ and $\mathcal{Y}_L > 0$ are convectively unstable.

2. Radiative Zones (RZs): Regions with $\mathcal{Y}_S < 0$ and $\mathcal{Y}_L \leq \mathcal{Y}_S$ are always stable to convection. Other combinations of \mathcal{Y}_L and \mathcal{Y}_S may also be RZs, as detailed below in #3 and #4.

3. “Semiconvection” Zones (SZs): Regions with $\mathcal{Y}_S > 0$ but $\mathcal{Y}_L < 0$ are stabilized to convection by a composition gradient despite an unstable thermal stratification. These regions can be stable RZs or linearly unstable to oscillatory double-diffusive convection (ODDC, see [Garaud 2018](#), chapters 2 and 4).

4. “Thermohaline” Zones: Regions with $\mathcal{Y}_S < 0$ and $\mathcal{Y}_L > \mathcal{Y}_S$ are thermally stable to convection despite an unstable composition gradient. These regions can be stable RZs or linearly unstable to thermohaline mixing (see [Garaud 2018](#), chapters 2 and 3).

In this letter, we study a three-layer 3D simulation of convection. The initial structure of the simulation is an unstable CZ (bottom, #1), a compositionally-stabilized SZ (middle, #3), and a thermally stable RZ (top, #2). We examine how the boundary of the CZ evolves through entrainment. In particular, we are interested in seeing if the roots of \mathcal{Y}_S and \mathcal{Y}_L coincide on timescales that are long compared to the dynamical timescale but short compared to evolutionary timescales.

In this work, we utilize a 3D model employing the Boussinesq approximation, which is formally valid when motions occur on length scales much smaller than the pressure scale height. This approximation fully captures the primary focus of this work, which is nonlinear advective mixing near the CZ-SZ boundary. Our simulations use a height-dependent ∇_{rad} and buoyancy is determined by a combination of the composition μ and the temperature stratification T , so \mathcal{Y}_S and \mathcal{Y}_L are determined independently and self-consistently. For details on our model setup and Dedalus simulations, we refer the reader to appendices A and B.

3. RESULTS

In Fig. 1, we visualize the composition field in our simulation near the initial state (left) and evolved state (right). Overplotted horizontal lines correspond to the convective boundaries via the Ledoux (orange, $\mathcal{Y}_L = 0$) and Schwarzschild (purple, $\mathcal{Y}_S = 0$) criteria. Initially, the bottom third of the domain is a CZ, the middle third is an SZ, and the top third is an RZ. Convection motions extend beyond $\mathcal{Y}_L = 0$ at all times; we refer to these motions as overshoot (which is discussed in [Korre et al. 2019](#)). Overshoot occurs because the Ledoux boundary is not the location where convective velocity is zero, but

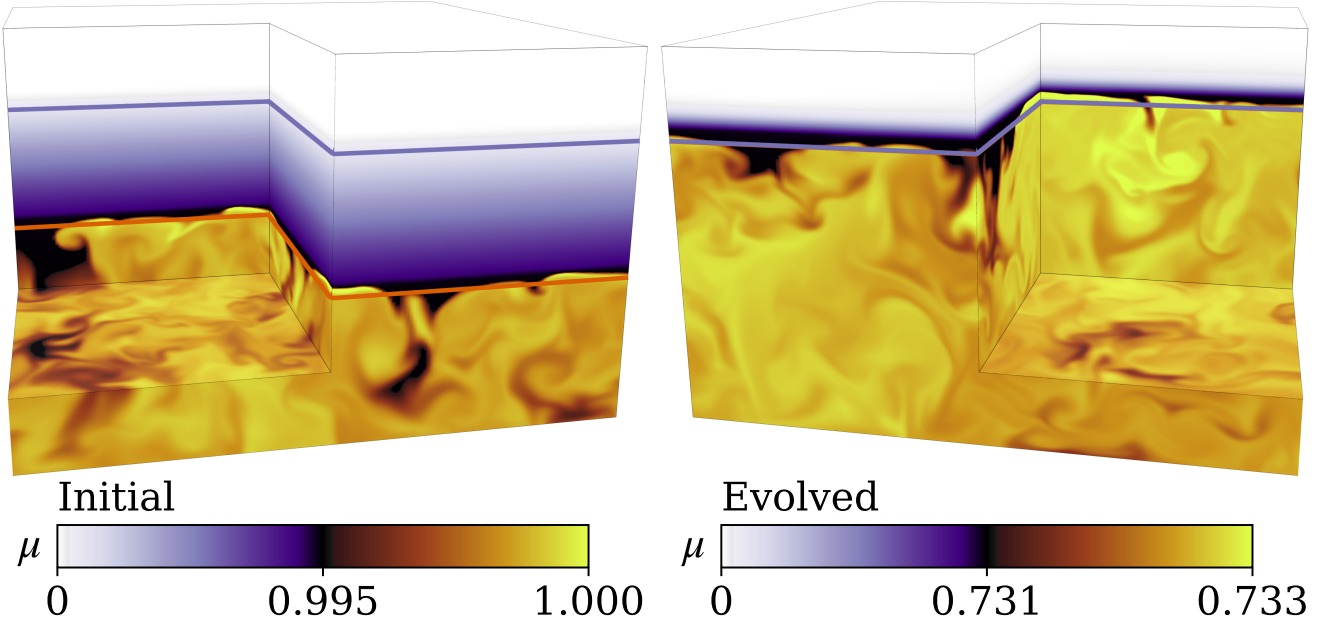


Figure 1. Volume renderings of the composition μ at early (left) and late (right) times. The change in color from white at the top of the box to dark purple at the top of the convection zone denotes a stable composition gradient. The convection zone is well-mixed, so we expand the colorbar scaling there; black represents entrained low- μ fluid being mixed into the yellow high- μ convection zone. The orange and purple horizontal lines respectively denote the heights at which $\mathcal{Y}_L = 0$ and $\mathcal{Y}_S = 0$. The two criteria are equivalent in the right panel, so the orange line is not visible. The simulation domain spans $z \in [0, 3]$, but we only plot $z \in [0, 2.5]$ here.

rather the location where buoyant acceleration changes sign due to a sign change in the entropy gradient.

The most obvious change from the left to the right panel is that the CZ has consumed the SZ and fills the bottom two-thirds of the box. Overshooting convective motions entrain low-composition material into the CZ where it is homogenized. This process increases the size of the CZ and repeats over thousands of convective overturn times until the Ledoux and Schwarzschild criteria predict the same convective boundary. After this “entrainment” phase, the convective boundary stops moving. The boundary is stable because the radiative flux renews and reinforces the stable temperature gradient; there is no analogous process to reinforce the composition gradient¹.

Figure 2 displays vertical simulation profiles in the initial (left) and evolved (right) states. Shown are the composition μ (top), the discriminants \mathcal{Y}_L and \mathcal{Y}_S (middle), and the square Brunt–Väisälä frequency (top) as well as the square convective frequency defined as

$$f_{\text{conv}}^2 = \frac{|\mathbf{u}|^2}{\ell_{\text{conv}}^2}, \quad (3)$$

¹ Nuclear timescales are generally much longer than dynamical timescales and can be neglected as a source of composition.

where $|\mathbf{u}|$ is the horizontally-averaged velocity magnitude and ℓ_{conv} is the depth of the convectively unstable layer.

Initially, the composition is uniform in the CZ ($z < 1$) and RZ ($z > 2$), but varies linearly in the SZ ($z \in [1, 2]$). We have $\mathcal{Y}_L(z = 1) \approx 0$ but $\mathcal{Y}_S(z = s) \approx 0$. The Brunt–Väisälä frequency N^2 is negative in a boundary layer at the base of the CZ which drives the instability. N^2 is stable for $z \gtrsim 1$, and is larger in the RZ than the SZ by an order of magnitude. We found similar results in simulations where N^2 was constant across the RZ and SZ.

In the evolved state (right panels), the composition profile (top) is constant in the CZ and overshoot zone (denoted as a transparent hashed region), but decreases abruptly at the top of the overshoot zone. The top of the hashed overshoot zone is taken to be the height where the horizontally-averaged kinetic energy falls below 10% of its bulk-CZ value. The Schwarzschild and Ledoux criteria agree upon the location of the convective boundary (middle).

Furthermore, in the CZ, the convective frequency is roughly constant and $N^2 \lesssim 0$ (bottom). In the RZ, $f_{\text{conv}}^2 \approx 0$ and $N^2 \gg 0$. We can compute the “stiffness”

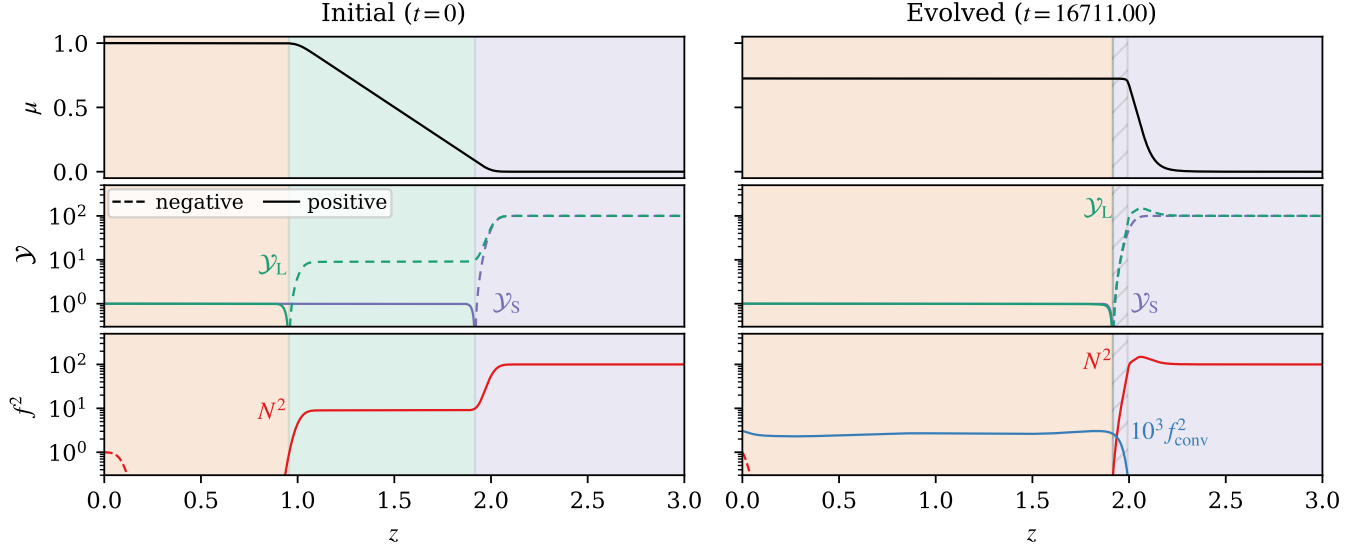


Figure 2. Horizontally-averaged profiles of the composition (top), the discriminants \mathcal{Y}_S and \mathcal{Y}_L (middle, Eqns. 1 & 2), and the Brunt–Väisälä frequency $N^2 = -\mathcal{Y}_L$ and the square convective frequency f_{conv}^2 (bottom, Eqn. 3). Positive and negative values are respectively solid and dashed lines. We show the initial (left) and evolved (right, time-averaged over 100 convective overturn times) states. There are no motions in the initial state, so $f_{\text{conv}}^2 = 0$ and does not appear. The background color is orange in CZs, green in SZs, and purple in RZs per Section 2. The lightly hashed background region in the evolved RZ is the mechanical overshoot zone.

199 of the radiative-convective interface,

$$\mathcal{S} = \frac{N^2|_{\text{RZ}}}{f_{\text{conv}}^2|_{\text{CZ}}}, \quad (4)$$

201 which is related to the Richardson number $\text{Ri} = \sqrt{\mathcal{S}}$.
 202 Convective boundaries in stars often have $\mathcal{S} \gtrsim 10^6$. Note
 203 that the time to entrain the SZ is roughly $\tau_{\text{entrain}} \sim$
 204 $(\delta h / \ell_{\text{conv}})^2 R_\rho^{-1} \mathcal{S} \tau_{\text{dyn}}$ (per Fuentes & Cumming 2020,
 205 eqn. 3), where δh is the depth of the SZ, ℓ_{conv} is the
 206 convective length scale, $R_\rho > 1$ in an SZ is the den-
 207 sity ratio (see Garaud 2018, eqn. 7), and τ_{dyn} is the
 208 dynamical timescale. Our simulation has $\mathcal{S} \sim 10^4$ and
 209 $R_\rho = 1/10$ in the entrainment phase, so it is in the same
 210 high- \mathcal{S} and low- R_ρ regime as stars. Since the relevant
 211 timescale of evolution on the main sequence is the nu-
 212 clear time τ_{nuc} , and since $\tau_{\text{nuc}} / \tau_{\text{dyn}} \gg (\delta h / \ell_{\text{conv}})^2 \mathcal{S} / R_\rho$
 213 even for $\mathcal{S} \sim 10^6$, we expect CZs to entrain SZs during
 214 a single stellar evolution time step. Note also that the
 215 low values of R_ρ present in SZs in stars can lead to ad-
 216 ditional instabilities which can cause them to mix faster
 217 than this estimate; we discuss this in Sec. 4.

218 Finally, Figure 3 displays a Kippenhahn-like diagram
 219 of the simulation’s evolution. This diagram demon-
 220 strates the evolution of the vertical extents of different
 221 dynamical regions. The convective boundary measure-
 222 ments are shown as orange ($\mathcal{Y}_L = 0$) and purple ($\mathcal{Y}_S = 0$)
 223 lines. The CZ is colored orange and fills the region below
 224 the Ledoux boundary, the RZ is colored purple and fills
 225 the region above the Schwarzschild boundary, and the

226 SZ is colored green and fills the region between these
 227 boundaries. Convection motions overshoot above the
 228 Ledoux boundary; the hashed zone corresponds to the
 229 same overshoot extent displayed in Fig. 2. The top of
 230 the overshoot zone, denoted by a black line, roughly
 231 correspond with the maximum of $\partial\mu/\partial z$ (Fig. 2, up-
 232 per right), so this describes overshoot well. While the
 233 Schwarzschild and Ledoux boundaries start at different
 234 heights, 3D convective mixing causes them to converge
 235 on dynamical timescales.

4. CONCLUSIONS & DISCUSSION

237 In this letter, we present a 3D simulation of a con-
 238 vection zone adjacent to a compositionally stable and
 239 weakly thermally unstable region. This region is stable
 240 according to the Ledoux criterion, but unstable accord-
 241 ing to the Schwarzschild criterion. Overshooting convec-
 242 tive motions entrain the entire Schwarzschild-unstable
 243 region until the Schwarzschild and Ledoux criterion both
 244 predict the same boundary of the convection zone.

245 This simulation demonstrates that, while the Ledoux
 246 criterion *instantaneously* predicts the location of
 247 the convective boundary, on evolutionary timescales
 248 ($t_{\text{evol}} \gg (\delta h / \ell_{\text{conv}})^2 R_\rho^{-1} \mathcal{S} \tau_{\text{dyn}}$, see Sec. 3) the convec-
 249 tive boundary is given by the Schwarzschild criterion.
 250 Our 3D simulation supports the claim that “logically
 251 consistent” implementations of mixing length theory
 252 (Gabriel et al. 2014; Paxton et al. 2018, 2019) should
 253 have convective boundaries which are Schwarzschild-

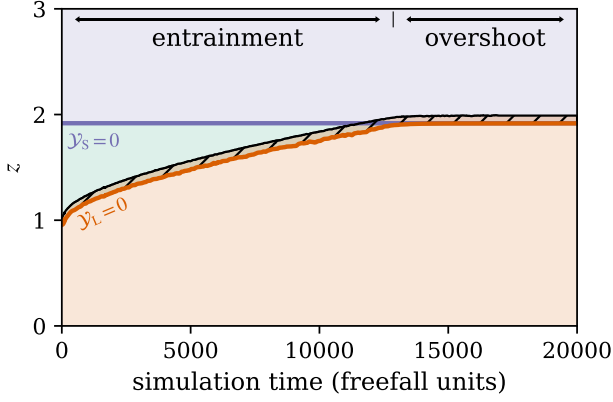


Figure 3. A Kippenhahn-like diagram of the simulation evolution. The y -axis is simulation height and the x -axis is simulation time. The orange line denotes the convective boundary according to the Ledoux criterion ($\mathcal{Y}_L = 0$); the CZ is below this and is colored orange. The purple line denotes the convective boundary according to the Schwarzschild criterion ($\mathcal{Y}_S = 0$); the RZ is above this and is colored purple. The semiconvective region between these boundaries is colored green. The overshoot zone is hashed, and the black line denotes the top of this region. The simulation has an “entrainment phase” while the CZ expands, and a pure “overshoot phase” where the convective boundary does not advance. *Note: The simulation has only evolved to $t = 17000$, and I extended the end of this; it is running to 20000.*

stable. E.g., the MESA software instrument’s “convective pre-mixing” (CPM, Paxton et al. 2019) is consistent with our simulation. The results of 1D stellar evolution calculations should not depend on the choice of stability criterion used when $t_{\text{evol}} \gg (\delta h / \ell_{\text{conv}})^2 R_\rho^{-1} S t_{\text{dyn}}$.

In many stars, the SZ is unstable to oscillatory double-diffusive convection (ODDC). ODDC mixes composition gradients even more rapidly than the entrainment studied here, and has been studied extensively in local simulations (Mirouh et al. 2012; Wood et al. 2013; Xie et al. 2017); see the review of Garaud (2018). Moore & Garaud (2016) apply ODDC to the regions outside core convection zones in main sequence stars, and their results suggest that ODDC formulations should

be widely included in stellar models. This letter shows that ODDC-unstable zones should not form at convective boundaries. However, if they did, they would likely be rapidly mixed by a combination of ODDC and entrainment.

For stages in stellar evolution where $(\delta h / \ell_{\text{conv}})^2 R_\rho^{-1} S t_{\text{dyn}} \sim t_{\text{evol}}$, implementations of time-dependent convection (TDC, Kuhfuss 1986) are required to better capture convective dynamics. These evolutionary stages should also implement time-dependent entrainment models to properly advance convective boundaries (e.g., Turner 1968; Fuentes & Cumming 2020).

Anders et al. (2021) showed convective motions can extend significantly into the radiative zones of stars via “penetrative convection.” In this work, we used parameters which do not have significant penetration. This can be seen because while the composition is well-mixed above the convective boundary, the thermal structure does not mix to the adiabatic.

We assume that the radiative conductivity and ∇_{rad} do not depend on μ for simplicity. The nonlinear feedback between these effects should be studied in future work, but we expect that our conclusions are robust.

We thank Meridith Joyce, Anne Thoul, Dominic Bowman, Jared Goldberg, Tim Cunningham, Falk Herwig, Kyle Augustson, (OTHERS?) for useful discussions which helped improve our understanding. EHA is funded as a CIERA Postdoctoral fellow and would like to thank CIERA and Northwestern University. AEF acknowledges support from NSF Grant Nos. AST-1814327 and AST-1908338. This research was supported in part by the National Science Foundation under Grant No. PHY-1748958, and we acknowledge the hospitality of KITP during the Probes of Transport in Stars Program. Computations were conducted with support from the NASA High End Computing (HEC) Program through the NASA Advanced Supercomputing (NAS) Division at Ames Research Center on Pleiades with allocation GID s2276. The Flatiron Institute is supported by the Simons Foundation.

APPENDIX

A. MODEL & INITIAL CONDITIONS

In this work we study incompressible, Boussinesq convection with a composition field. These equations are

$$\nabla \cdot \mathbf{u} = 0 \quad (\text{A1})$$

$$\partial_t \mathbf{u} + \mathbf{u} \cdot \nabla \mathbf{u} + \nabla \varpi = \left(T - \frac{\mu}{R_\rho} \right) \hat{z} + \frac{\text{Pr}}{\text{Pe}} \nabla^2 \mathbf{u}, \quad (\text{A2})$$

$$\partial_t T + \mathbf{u} \cdot (\nabla T - \hat{z} \partial_z T_{\text{ad}}) + \nabla \cdot [-\kappa_{T,0} \nabla \bar{T}] = \frac{1}{\text{Pe}} \nabla^2 T', \quad (\text{A3})$$

$$\partial_t \mu + \mathbf{u} \cdot \nabla \mu = \frac{\tau_0}{\text{Pe}} \nabla^2 \bar{\mu} + \frac{\tau}{\text{Pe}} \nabla^2 \mu'. \quad (\text{A4})$$

Here, \mathbf{u} is velocity, T is temperature, and μ is concentration. Bars (e.g., \bar{T}) represent the horizontally-averaged component of a field and primes (e.g., T') denote all fluctuations around that background. The adiabatic temperature gradient is $\partial_z T_{\text{ad}}$ and the nondimensional con-

trol parameters are

$$\begin{aligned} \text{Pe} &= \frac{u_{\text{ff}} \ell_{\text{conv}}}{\kappa_T}, & R_\rho &= \frac{|\alpha| \Delta T}{|\beta| \Delta \mu}, \\ \text{Pr} &= \frac{\nu}{\kappa_T}, & \tau &= \frac{\kappa_\mu}{\kappa_T}, \end{aligned} \quad (\text{A5})$$

where the nondimensional freefall velocity is $u_{\text{ff}} = \sqrt{|\alpha| g \ell_{\text{conv}} \Delta T}$ (with gravitational acceleration g), ℓ_{conv} is the initial depth of the convection zone, $\Delta \mu$ is the composition change across the Ledoux stable region, $\Delta T = \ell_{\text{conv}} (\partial_z T_{\text{rad}} - \partial_z T_{\text{ad}})$ is the superadiabatic temperature scale of the convection zone, α and β are the coefficients of expansion for T and μ , ν is the viscosity, κ_T is the thermal diffusivity, and κ_μ is the compositional diffusivity. Eqns. A1-A4 are identical to Eqns. 2-5 in [Garaud \(2018\)](#), except we modify the diffusion coefficients acting on \bar{T} ($\kappa_{T,0}$) and $\bar{\mu}$ (τ_0). By doing this, we keep the turbulence (Pe) uniform throughout the domain while also allowing the radiative temperature gradient $\partial_z T_{\text{rad}} = -\text{Flux}/\kappa_{T,0}$ to vary with height. We furthermore reduce diffusion on $\bar{\mu}$ to ensure its evolution is due to advection.

We define the Ledoux and Schwarzschild discriminants

$$\mathcal{Y}_S = \left(\frac{\partial T}{\partial z} \right)_{\text{rad}} - \left(\frac{\partial T}{\partial z} \right)_{\text{ad}}, \quad \mathcal{Y}_L = \mathcal{Y}_S - R_\rho^{-1} \frac{\partial \mu}{\partial z}, \quad (\text{A6})$$

and in this nondimensional system the Brunt-Väisälä frequency is the negative of the Ledoux discriminant $N^2 = -\mathcal{Y}_L$.

We study a three-layer model with $z \in [0, 3]$,

$$\left(\frac{\partial T}{\partial z} \right)_{\text{rad}} = \left(\frac{\partial T}{\partial z} \right)_{\text{ad}} + \begin{cases} -1 & z \leq 2 \\ 10R_\rho^{-1} & z > 2 \end{cases}, \quad (\text{A7})$$

$$\frac{\partial \mu_0}{\partial z} = \begin{cases} 0 & z \leq 1 \\ -1 & 1 < z \leq 2 \\ 0 & z > 2 \end{cases}, \quad (\text{A8})$$

We set $\mu = 1$ at $z = 0$ and $T = 1$ at $z = 3$. The initial temperature profile has $\partial_z T_0 = \partial_z T_{\text{rad}}$ everywhere

except between $z = [0.1, 1]$ where $\partial_z T_0 = \partial_z T_{\text{ad}}$. We set $(\partial T / \partial z)_{\text{ad}} = -1 - 10R_\rho^{-1}$. To obtain μ_0 , we numerically integrate Eqn. A8 with $\mu_0(z = 0) = 0$. To obtain T_0 , we numerically integrate $\partial_z T_0 = (\partial_z T)_{\text{rad}}$ (Eqn. A7) with $T_0(z = 3) = 1$.

B. SIMULATION DETAILS & DATA AVAILABILITY

We time-evolve equations A1-A4 using the Dedalus pseudospectral solver ([Burns et al. 2020](#), git commit 1339061) using timestepper SBDF2 ([Wang & Ruuth 2008](#)) and safety factor 0.3. All variables are represented using a Chebyshev series with 512 terms for $z \in [0, 2.25]$, another Chebyshev series with 64 terms for $z \in [2.25, 3]$, and Fourier series in the periodic x and y directions with 192 terms each. Our domain spans $x \in [0, L_x]$, $y \in [0, L_y]$, and $z \in [0, L_z]$ with $L_x = L_y = 4$ and $L_z = 3$. To avoid aliasing errors, we use the 3/2-dealiasing rule in all directions. To start our simulations, we add random noise temperature perturbations with a magnitude of 10^{-6} to the initial temperature profile.

Spectral methods with finite coefficient expansions cannot capture true discontinuities. To approximate discontinuous functions such as Eqns. A7 & A8, we define a smooth Heaviside step function centered at $z = z_0$,

$$H(z; z_0, d_w) = \frac{1}{2} \left(1 + \text{erf} \left[\frac{z - z_0}{d_w} \right] \right). \quad (\text{B9})$$

where erf is the error function and we set $d_w = 0.05$. The simulation in this work uses $\mathcal{P} = 3.2 \times 10^3$, $R_\rho^{-1} = 10$, $\text{Pr} = \tau = 0.5$, $\tau_0 = 1.5 \times 10^{-3}$, and $\kappa_{T,0} = \mathcal{P}^{-1} [(\partial T / \partial z)_{\text{rad}}|_{z=0}] / (\partial T / \partial z)_{\text{rad}}$

We produced figures 2 and 3 using matplotlib ([Hunter 2007](#); [Caswell et al. 2021](#)). We produced figure 1 using plotly ([Inc. 2015](#)) and matplotlib. All of the Python scripts used to run the simulations in this paper and to create the figures in this paper are publicly available in a git repository (https://github.com/evanhanders/schwarzschild_or_ledoux) and in a Zenodo repository ([?](#)).

REFERENCES

- Anders, E. H., Jermyn, A. S., Lecoanet, D., & Brown, B. P. 2021, arXiv e-prints, arXiv:2110.11356. <https://arxiv.org/abs/2110.11356>
- Andrassy, R., Herwig, F., Woodward, P., & Ritter, C. 2020, MNRAS, 491, 972, doi: [10.1093/mnras/stz2952](https://doi.org/10.1093/mnras/stz2952)
- Andrassy, R., Higl, J., Mao, H., et al. 2021, arXiv e-prints, arXiv:2111.01165. <https://arxiv.org/abs/2111.01165>
- Basu, S. 2016, Living Reviews in Solar Physics, 13, 2, doi: [10.1007/s41116-016-0003-4](https://doi.org/10.1007/s41116-016-0003-4)
- Basu, S., Verner, G. A., Chaplin, W. J., & Elsworth, Y. 2012, ApJ, 746, 76, doi: [10.1088/0004-637X/746/1/76](https://doi.org/10.1088/0004-637X/746/1/76)
- Burns, K. J., Vasil, G. M., Oishi, J. S., Lecoanet, D., & Brown, B. P. 2020, Physical Review Research, 2, 023068, doi: [10.1103/PhysRevResearch.2.023068](https://doi.org/10.1103/PhysRevResearch.2.023068)

- 404 Carlos, M., Meléndez, J., Spina, L., et al. 2019, MNRAS,
405 485, 4052, doi: [10.1093/mnras/stz681](https://doi.org/10.1093/mnras/stz681)
- 406 Caswell, T. A., Droettboom, M., Lee, A., et al. 2021,
407 matplotlib/matplotlib: REL: v3.3.4, v3.3.4, Zenodo,
408 doi: [10.5281/zenodo.4475376](https://doi.org/10.5281/zenodo.4475376)
- 409 Claret, A., & Torres, G. 2018, ApJ, 859, 100,
410 doi: [10.3847/1538-4357/aabd35](https://doi.org/10.3847/1538-4357/aabd35)
- 411 Cristini, A., Hirschi, R., Meakin, C., et al. 2019, MNRAS,
412 484, 4645, doi: [10.1093/mnras/stz312](https://doi.org/10.1093/mnras/stz312)
- 413 Dumont, T., Palacios, A., Charbonnel, C., et al. 2021,
414 A&A, 646, A48, doi: [10.1051/0004-6361/202039515](https://doi.org/10.1051/0004-6361/202039515)
- 415 Farmer, R., Renzo, M., de Mink, S. E., Marchant, P., &
416 Justham, S. 2019, ApJ, 887, 53,
417 doi: [10.3847/1538-4357/ab518b](https://doi.org/10.3847/1538-4357/ab518b)
- 418 Fuentes, J. R., & Cumming, A. 2020, Physical Review
419 Fluids, 5, 124501, doi: [10.1103/PhysRevFluids.5.124501](https://doi.org/10.1103/PhysRevFluids.5.124501)
- 420 Gabriel, M., Noels, A., Montalbán, J., & Miglio, A. 2014,
421 A&A, 569, A63, doi: [10.1051/0004-6361/201423442](https://doi.org/10.1051/0004-6361/201423442)
- 422 Garaud, P. 2018, Annual Review of Fluid Mechanics, 50,
423 275, doi: [10.1146/annurev-fluid-122316-045234](https://doi.org/10.1146/annurev-fluid-122316-045234)
- 424 Georgy, C., Saio, H., & Meynet, G. 2021, A&A, 650, A128,
425 doi: [10.1051/0004-6361/202040105](https://doi.org/10.1051/0004-6361/202040105)
- 426 Hunter, J. D. 2007, Computing in Science and Engineering,
427 9, 90, doi: [10.1109/MCSE.2007.55](https://doi.org/10.1109/MCSE.2007.55)
- 428 Inc., P. T. 2015, Collaborative data science, Montreal, QC:
429 Plotly Technologies Inc. <https://plot.ly>
- 430 Johnston, C. 2021, A&A, 655, A29,
431 doi: [10.1051/0004-6361/202141080](https://doi.org/10.1051/0004-6361/202141080)
- 432 Jones, S., Andrassy, R., Sandalski, S., et al. 2017, MNRAS,
433 465, 2991, doi: [10.1093/mnras/stw2783](https://doi.org/10.1093/mnras/stw2783)
- 434 Kaiser, E. A., Hirschi, R., Arnett, W. D., et al. 2020,
435 MNRAS, 496, 1967, doi: [10.1093/mnras/staa1595](https://doi.org/10.1093/mnras/staa1595)
- 436 Korre, L., Garaud, P., & Brummell, N. H. 2019, MNRAS,
437 484, 1220, doi: [10.1093/mnras/stz047](https://doi.org/10.1093/mnras/stz047)
- 438 Kuhfuss, R. 1986, A&A, 160, 116
- 439 Meakin, C. A., & Arnett, D. 2007, ApJ, 667, 448,
440 doi: [10.1086/520318](https://doi.org/10.1086/520318)
- 441 Mehta, A. K., Buonanno, A., Gair, J., et al. 2022, ApJ,
442 924, 39, doi: [10.3847/1538-4357/ac3130](https://doi.org/10.3847/1538-4357/ac3130)
- 443 Mirouh, G. M., Garaud, P., Stellmach, S., Traxler, A. L., &
444 Wood, T. S. 2012, ApJ, 750, 61,
445 doi: [10.1088/0004-637X/750/1/61](https://doi.org/10.1088/0004-637X/750/1/61)
- 446 Moore, K., & Garaud, P. 2016, ApJ, 817, 54,
447 doi: [10.3847/0004-637X/817/1/54](https://doi.org/10.3847/0004-637X/817/1/54)
- 448 Morrell, S. A. F. 2020, PhD thesis, University of Exeter
- 449 Paxton, B., Schwab, J., Bauer, E. B., et al. 2018, ApJS,
450 234, 34, doi: [10.3847/1538-4365/aaa5a8](https://doi.org/10.3847/1538-4365/aaa5a8)
- 451 Paxton, B., Smolec, R., Schwab, J., et al. 2019, ApJS, 243,
452 10, doi: [10.3847/1538-4365/ab2241](https://doi.org/10.3847/1538-4365/ab2241)
- 453 Pedersen, M. G., Aerts, C., Pápics, P. I., et al. 2021, arXiv
454 e-prints, arXiv:2105.04533.
455 <https://arxiv.org/abs/2105.04533>
- 456 Pinsonneault, M. 1997, ARA&A, 35, 557,
457 doi: [10.1146/annurev.astro.35.1.557](https://doi.org/10.1146/annurev.astro.35.1.557)
- 458 Salaris, M., & Cassisi, S. 2017, Royal Society Open Science,
459 4, 170192, doi: [10.1098/rsos.170192](https://doi.org/10.1098/rsos.170192)
- 460 Scott, L. J. A., Hirschi, R., Georgy, C., et al. 2021,
461 MNRAS, 503, 4208, doi: [10.1093/mnras/stab752](https://doi.org/10.1093/mnras/stab752)
- 462 Sestito, P., & Randich, S. 2005, A&A, 442, 615,
463 doi: [10.1051/0004-6361:20053482](https://doi.org/10.1051/0004-6361:20053482)
- 464 Staritsin, E. I. 2013, Astronomy Reports, 57, 380,
465 doi: [10.1134/S1063772913050089](https://doi.org/10.1134/S1063772913050089)
- 466 Turner, J. S. 1968, Journal of Fluid Mechanics, 33, 183,
467 doi: [10.1017/S0022112068002442](https://doi.org/10.1017/S0022112068002442)
- 468 Viani, L. S., & Basu, S. 2020, ApJ, 904, 22,
469 doi: [10.3847/1538-4357/abba17](https://doi.org/10.3847/1538-4357/abba17)
- 470 Wang, D., & Ruuth, S. J. 2008, Journal of Computational
471 Mathematics, 26, 838.
472 <http://www.jstor.org/stable/43693484>
- 473 Wood, T. S., Garaud, P., & Stellmach, S. 2013, ApJ, 768,
474 157, doi: [10.1088/0004-637X/768/2/157](https://doi.org/10.1088/0004-637X/768/2/157)
- 475 Woodward, P. R., Herwig, F., & Lin, P.-H. 2015, ApJ, 798,
476 49, doi: [10.1088/0004-637X/798/1/49](https://doi.org/10.1088/0004-637X/798/1/49)
- 477 Xie, J.-H., Miquel, B., Julien, K., & Knobloch, E. 2017,
478 Fluids, 2, doi: [10.3390/fluids2010006](https://doi.org/10.3390/fluids2010006)